Enhanced Photoresponse of FeS_2 Films: The Role of Marcasite–Pyrite Phase Junctions

*Longfei Wu, Nelson Y. Dzade, Lu Gao, David O. Scanlon, Zafer Öztürk, Nathan Hollingsworth, Bert M. Weckhuysen, Emiel J. M. Hensen, Nora H. de Leeuw, and Jan P. Hofmann**

The interest in iron pyrite (cubic FeS_2) as a photovoltaic material has increased significantly recently, because of its earth-abundancy, nontoxicity, and its suitable band gap (≈0.95 eV) for solar cell applications.[1–4] Moreover, the large photon absorption coefficient of 10^5 cm^{-1} (two orders of magnitude higher than that of crystalline silicon), high carrier mobility as well as its outstanding theoretical power conversion efficiency of 28% (according to the Shockley–Queisser model) make pyrite a competitive candidate in the development of sustainable and inexpensive solar cells at the terawatt scale.[1,5] Since the early 1990s, extensive efforts from Tributsch and co-workers and other groups have been devoted to iron pyrite photoelectrochemical and Schottky-type solar cells.[6–10] Besides, the distinct chemical and physical properties of pyrite also make it a suitable candidate for photodetectors,[1b] anode materials for lithium-ion batteries,[1c] photocatalysis,[5b] photocapacitors,[5c] hydrogen production, and photoelectrochemical (PEC) cells.[5d] Although photovoltaic cells based on pyrite single crystals show large photocurrent densities (>30 mA cm^{-2}) and high quantum efficiencies (>90%), the low open-circuit voltage (V_{OC}) of 200 mV limits their solar energy conversion efficiency to ≈3%. Despite the fact that a lot of attempts such as morphology control or ligand protection have been tried,[11b–d] the device efficiency has not improved significantly in the past 20 years.[1,6,12,11,13,14] Several possible explanations have been suggested for the low V_{OC}, including bulk non-stoichiometry,[7,15–17] near-surface non-stoichiometry (resulting in a metallic FeS-like surface layer),[18] sulfur vacancies that generate electronic states in the band gap,[13] Fermi level pinning induced by surface states,[19] or small band gap phases (pyrrhotite, troilite, and marcasite) present as domains in bulk pyrite.[8] Orthorhombic marcasite (FeS_2) and hexagonal troilite (FeS) are believed to be detrimental phases for photochemical performance, as they have much smaller band gaps (0.04 eV for troilite and 0.34 eV for marcasite),[20] and it has been suggested that even trace amounts of these phases would cause the low V_{OC} reported for pyrite films.[21] The band gap of marcasite was first determined from temperature-dependent (53–370 K) electrical resistivity measurements and a value of 0.34 eV was obtained.[20] However, these measurements were based on the assumption that the carrier mobility is dominated by lattice scattering,[20,22] and the band gap value of marcasite has been rarely verified by other methods, such as optical measurements. Furthermore, several theoretical calculations published in recent years predict that marcasite should have a band gap of 0.8–1.0 eV, which is quite similar to that of pyrite; Gudelli even observed that marcasite has a much larger band gap than pyrite (1.603 eV for marcasite and 1.186 eV for pyrite).[23,24] Very recently, the optical band gap energy of marcasite has been determined by diffuse reflectance spectroscopy to be 0.83 ± 0.02 eV, and the optical absorption of marcasite and pyrite in the near infrared–visible (NIR–Vis) region appears to be quite similar.[25] Therefore, the presence of marcasite is unlikely to undermine the photovoltaic performance of pyrite and it is therefore worth considering whether significant effort should actually be expended on eliminating marcasite traces from pyrite preparations. As the formation of junctions (such as p–n junctions or phase junctions) can efficiently promote charge separation in semiconductor-based photocatalysts, the fabrication of proper junctions in semiconductors is highly desirable in the design and preparation of efficient semiconductor-based photocatalysts. The most conspicuous example is the activity of TiO_2 (P-25, Degussa), which consists of anatase and rutile (4:1 w/w) and exceeds the photocatalytic activity of pure anatase in many reaction systems.[26–32] Furthermore, Li and co-workers have reported enhanced photocatalytic performance of Ga_2O_3 with tunable α-β phase junctions. The drastically enhanced activity of mixed α- and β-Ga_2O_3 over the phase pure oxides was ascribed to efficient charge separation and transfer across the α-β phase junctions.[33–35] As to the pyrite-marcasite interface, although most published work has attributed the low performance of pyrite films to the minor presence of marcasite, no

L. Wu, Dr. L. Gao, Prof. E. J. M. Hensen, Dr. J. P. Hofmann
Laboratory of Inorganic Materials Chemistry
Department of Chemical Engineering and Chemistry
Eindhoven University of Technology
P.O. Box 513, 5600 MB, Eindhoven, The Netherlands
E-mail: j.p.hofmann@tue.nl
Dr. N. Y. Dzade, Prof. N. H. de Leeuw
Faculty of Geosciences
Utrecht University
Princetonplein 9, 3584 CC, Utrecht, The Netherlands
Dr. D. O. Scanlon, Dr. N. Hollingsworth
Department of Chemistry
University College London
20 Gordon Street, London WC1H0AJ, UK
Z. Öztürk, Prof. B. M. Weckhuysen
Inorganic Chemistry and Catalysis
Debye Institute for Nanomaterials Science
Utrecht University
Universiteitsweg 99, 3584 CG, Utrecht, The Netherlands

DOI: 10.1002/adma.201602222

interfacial gap states have been found by examining the density of states (DOS) at the pyrite-marcasite interface and the band gap of the pyrite–marcasite supercell was not smaller than the isolated pyrite gap.[36] Moreover, according to theoretical calculations, the stability of marcasite is much better than pyrite.[37–39]

In this communication, we present FeS_2 films with mixed pyrite-marcasite phase junctions prepared by sulfurization of sputtered Fe thin layers on highly doped Si wafers. The mixed phase films show highly improved photocurrents at 0.5 V vs. Hg/Hg_2SO_4 of 4.30 mA cm^{-2} compared to 0.14 mA cm^{-2} of phase pure pyrite films. Apart from the considerably improved photoresponse, the dark current is greatly reduced. Furthermore, the presence of marcasite significantly increased the stability of the film against photo-corrosion. Thus, in contrast to the traditional view that marcasite is a detrimental phase for the low V_{OC} of pyrite-based solar cells, our experimental results suggest that marcasite is beneficial for the charge separation and stability of pyrite films. We propose that the enhanced performance is owing to the efficient charge separation across the pyrite–marcasite (p/m-FeS_2) phase junction. This hypothesis is corroborated through state-of-the-art calculations based on the density functional theory (DFT) with Hubbard corrections for the electron correlation in the localized *d*-Fe orbitals (DFT+U), where we find that a staggered band alignment with offsets of 0.43 and 0.71 eV exists between the valence and conduction bands of marcasite and pyrite, respectively. This staggered alignment with both bands of marcasite higher in energy than pyrite indicates that photo-generated conduction band electrons will flow from marcasite to pyrite and vice versa for photo-generated valence band holes in mixed-phase FeS_2 thin films. These findings point to efficient charge separation in the mixed systems as the primary origin of the observed high photo-activity (photocurrent) of the mixed marcasite–pyrite thin films over the individual pyrite counterpart.

We have adopted a unique synthesis strategy in which Fe/Si films are placed at certain distances from the center of the furnace (Figure S1, Supporting Information), as such approach turned out to be beneficial in avoiding resublimation of evaporated sulfur in the upstream due to the temperature gradient of the furnace during low temperature sulfurization process. The temperature of the sulfurization was altered by varying the position of the Fe/Si films. Primarily, we aimed to make phase pure p-FeS_2 via optimization of the sulfurization temperature and time and three temperatures were chosen: 400, 500, and 600 °C. Scanning electron microscopy (SEM) images of the FeS_2 films obtained (Figure S2, Supporting information) indicate that varying the temperature from 400–600 °C results in particulate films with a continuous coverage at 400–500 °C, with the coverage becoming discontinuous by 600 °C. Energy dispersive X-ray spectroscopy (EDX) composition analysis confirmed that films sulfurized at 500 °C have the optimal stoichiometric Fe:S ratio. The cross-sectional SEM image of the film shows a final film thickness of 350 ± 20 nm (Figure S2, Supporting Information) and the calculated expansion factor (≈3.5) lies close to theoretical estimates for Fe to FeS_2 conversion.[40] X-ray diffraction (XRD), Raman spectroscopy, and X-ray photoelectron spectroscopy (XPS) all confirmed the films to be phase-pure p-FeS_2 (Figures S3–S4, Supporting Information). In addition, we also extended the sulfurization time at 500 °C to obtain higher film crystallinity, although XRD patterns and Raman spectra of pyrite films (Figures S5–S6, Supporting information) did not show significant differences between 5 h and longer annealing times. The indirect and direct optical band gaps of the pyrite films were determined by UV–Vis–NIR diffuse reflectance spectroscopy (Figure S7, Supporting information) to be 0.96 and 2.38 eV, respectively.

The previous sulfurization temperature only produced pyrite (p-FeS_2), as marcasite (m-FeS_2) can readily convert to p-FeS_2 at elevated temperatures under vacuum (or sulfur atmosphere),[41] but it is in principle possible to synthesize m-FeS_2 phase at lower sulfurization temperature.[40,42] Thus, sulfurization was performed on Fe/Si thin films at 300, 380, and 455 °C. XRD patterns were recorded for Fe films sulfurized at 300, 380, and 455 °C, respectively (Figure S8, Supporting Information).

The XRD signature of pyrite can be observed in all three samples, although the peak intensities decrease and become even inconspicuous with lower sulfurization temperature. Owing to the greater sensitivity of Raman spectroscopy to m-FeS_2 (Figure S9, Supporting Information), we observe an increase of marcasite peak intensity as the sulfurization temperature decreases. SEM images (Figure S9, Supporting Information) of the films show a decrease in particle size as the temperature is increased, which is understandable given the higher temperatures favor Ostwald ripening. In order to get better insight into the local phase distribution of marcasite and pyrite in the p/m-FeS_2 films, we performed Raman microspectroscopic imaging. **Figure 1**a,d,g shows the fitted Raman spectra of the FeS_2 films, where we observe all three separate Raman peaks from pyrite: predominant bands at 342.2 cm^{-1} (E_g, S_2 libration) and 378.1 cm^{-1} (A_{1g}, S-S in-phase stretch), and a minor peak at 429.6 cm^{-1} ($T_{g(3)}$ mode).[43–45] The band at 494.5 cm^{-1} has been assigned to coupled vibration and stretching (T_g) modes and combinations thereof.[46] The distinct marcasite band at 315–325 cm^{-1} (A_g) is only present in films sulfurized at 380 and 300 °C. The Raman intensity map in Figure 1 shows the phase distribution of pyrite and marcasite based on the fitted peak areas for the pyrite A_g band (b, e, h) in green and the marcasite peak (f, i) in red. According to Raman mapping, pyrite and marcasite are on a sub-μm scale uniformly distributed in the film, which implies that plenty of p/m-FeS_2 phase boundaries have been created. Moreover, it can be concluded that the lower the sulfurization temperature, the higher the marcasite content.

The photoelectrochemical properties of the as-obtained FeS_2 films were measured and evaluated for PEC applications. As shown in **Figure 2**, phase pure pyrite film has noticeable photocurrent in the positive voltage range under AM 1.5G illumination in 0.5 M KI aqueous solution. However, p/m-FeS_2 mixed phase films (p/m-FeS_2-380 °C and p/m-FeS_2-300 °C) show remarkably high photocurrents compared to phase-pure p-FeS_2 (p-FeS_2-455 °C).

The prominent high performance of p/m-FeS_2-380 °C can be explained by that an optimal phase mixture is needed while either higher (p/m-FeS_2-300 °C) or no (p-FeS_2-455 °C) marcasite content would lower the performance of FeS_2 films. Moreover, the dark current is greatly suppressed in p/m-FeS_2-380 and p/m-FeS_2-300 °C. Such a performance is unprecedented in polycrystalline pyrite films reported up to date.[4] To the best of our knowledge, this study is the first report of high

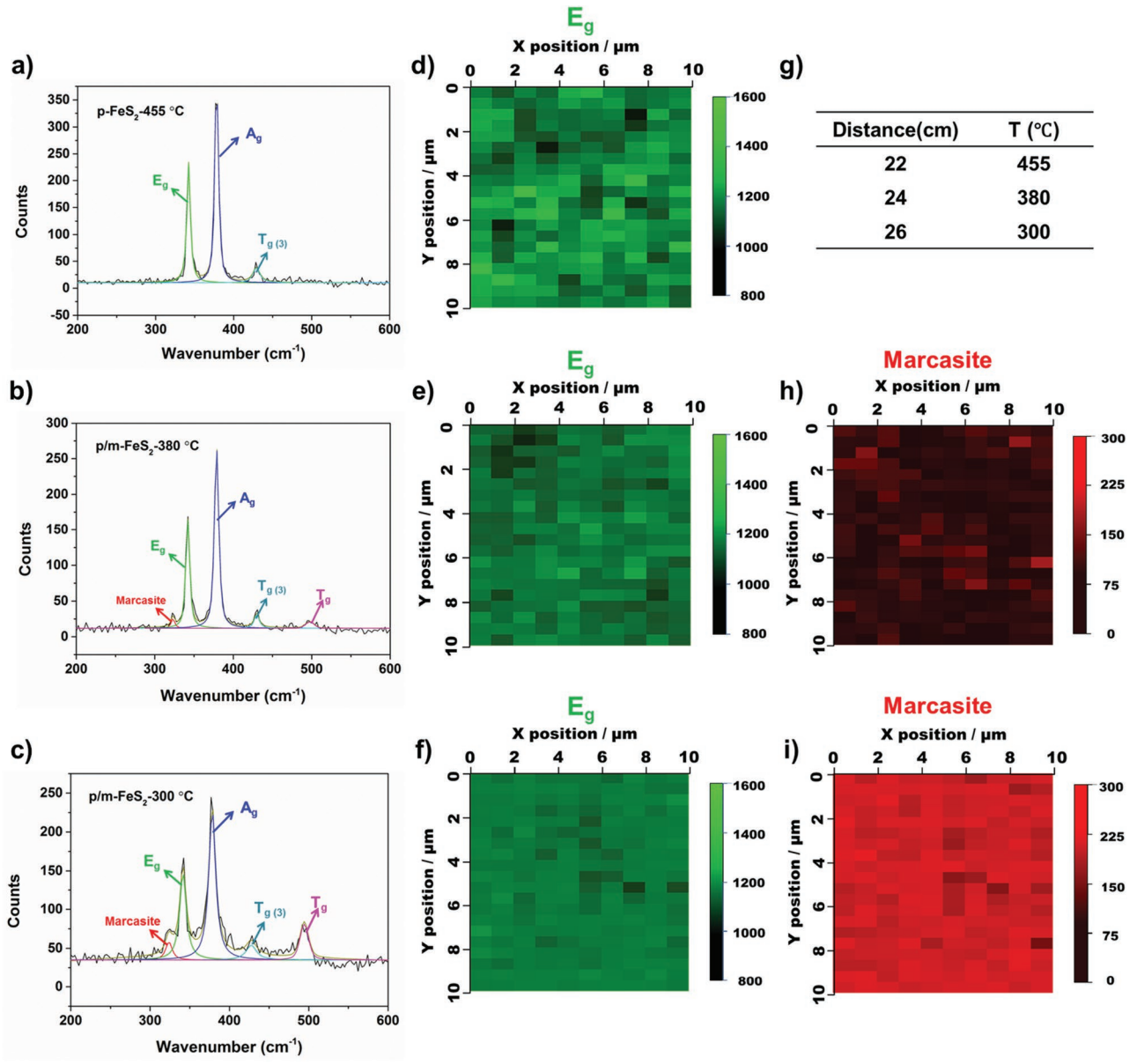

Figure 1. Fitted Raman spectra of FeS_2 films annealed at a) 455 °C, b) 380 °C, and c) 300 °C. Raman mapping of pyrite E_g (342 cm^{-1}) peak area of FeS_2 films annealed at d) 455 °C, e) 380 °C, and f) 300 °C. g) Sulfurization temperature of FeS_2 corresponding to different distances to the center of the furnace. Raman mapping of marcasite (≈320 cm^{-1}) peak area of FeS_2 films annealed at h) 380 °C and i) 300 °C.

performance mixed phase p/m-FeS_2 films and it reverses the common view that marcasite is detrimental for the photoperformance of pyrite films.

To investigate the fundamental mechanisms causing the highly improved p/m-FeS_2 films, we have carried out two separate computational analyses on both polymorphs: the electronic structures of the bulk crystals and the absolute vacuum alignment from a well converged slab-gap model (≈16 Å slab, 15 Å vacuum). First, we calculated the electronic band structure and density of states projected on the Fe *d*-states and S *p*-states for both orthorhombic marcasite and cubic pyrite using the generalized gradient approximation (GGA) with the Perdew, Burke and Ernzerhof (PBE) functional,[47] including a suitably determined Hubbard correction[48] (PBE+U) to account for the electron correlation in the localized *d*-Fe orbitals. We used an effective U of 2 eV for both materials, which has been shown to give a good description of the structure and electronic properties of FeS_2.[36,49–52]

The results are shown in **Figure 3** and full calculation details are provided in the Supporting Information. An analysis of the band structures revealed that the conduction band minimum (CBM) and valence band maximum (VBM), which in both materials are composed mainly of the Fe 3*d* states, are located at two different high-symmetry points in the Brillouin zone, making marcasite and pyrite indirect band gap semiconductors. The calculated band gap of marcasite is found to be

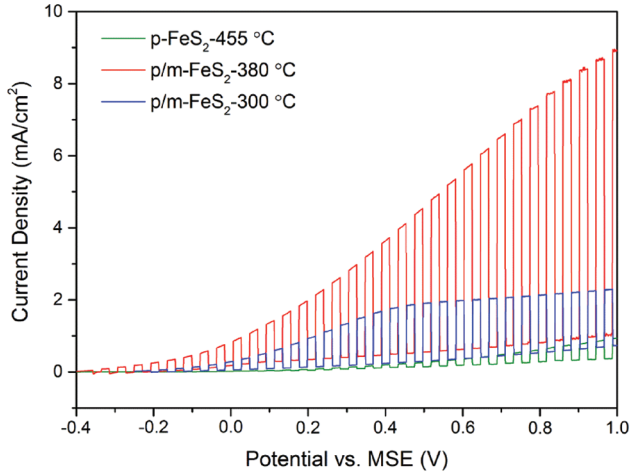

Figure 2. Chopped light voltammetry curves of FeS_2 films annealed at different temperatures (300 °C – blue; 380 °C – red; 455 °C – green) in 0.5 M KI aqueous solution versus Hg/Hg_2SO_4 (MSE) under 100 mW cm^{-2} AM 1.5G illumination.

1.17 eV and in pyrite it is 0.96 eV. The band gaps calculated from the present study are similar to the results obtained from a number of earlier theoretical investigations for marcasite[36,53] and pyrite.[36,54,55] In the case of pyrite, photoconductivity measurements show a consistent band gap in the range of 0.90–1.00 eV.[7,56]

Pyrite (100) and marcasite (110) surfaces were chosen for the slab calculations as these planes do not contain any dangling bonds and resulted in low energy, nonpolar terminations (Figure S16, Supporting Information). Besides, due to their structural similarities, intergrowth (epitaxial growth) of marcasite in (on) pyrite has been widely observed in synthetic and natural samples.[25,22,57–59] Our calculated work function of p-FeS_2(100) (Φ = 5.08 eV) also compares favorably with that of m-FeS_2(101) (Φ = 5.10 eV), which indicates the possibility of a barrier-less or low-barrier interface at the pyrite–marcasite junction. The calculated work function of p-FeS_2(100) is in excellent agreement with the value of 5.0 eV from ultraviolet photoelectron spectroscopy measurements.[7,4] The slab thickness was checked for convergence with respect to the vacuum potential. The models consistently predict an offset of 0.43 eV between marcasite and pyrite, with the marcasite valence band higher in energy than pyrite. The ionization potential (IP), which indicates the position where the valence band edge is observed, is calculated at 5.20 eV for marcasite and 5.63 eV for pyrite. In addition, our calculations demonstrate that the electron affinity (EA) of pyrite (4.71 eV) is higher than marcasite (4.00 eV), which indicates that photo-generated electrons will flow from marcasite to pyrite and vice versa for photo-generated valence holes as shown in **Figure 4**.

In addition to the photoresponse, the stability of the p/m-FeS_2-300 °C film under light illumination was evaluated (Figure S14, Supporting Information), which shows similar photoresponse after 4 d exposure to air, whereas the transient photoresponse under intermittent 1 sun illumination shows no activity degradation during the measurement over 30 min. Nevertheless, phase pure pyrite films show negligible photoresponse after 3 d exposure to air (Figure S16, supporting information). Such prominent improvement in stability can be explained by the band alignment between p-FeS_2 and m-FeS_2 at the interfaces, where electrons migrate to p-FeS_2 and contribute to its stability, keeping it in its reduced state. Furthermore, the enhanced stability can also be related to the lower unit cell energy of marcasite as has been shown in theoretical studies.[37]

In summary, we report for the first time the beneficial role of marcasite in iron sulfide-based photo-electrochemical applications. A novel strategy is adopted for fabricating mixed phase p/m-FeS_2 films, where the marcasite content can be tuned by controlling the sulfurization temperature. The dramatic improvement of the photoresponse of p/m-FeS_2 can be ascribed to the presence of pyrite–marcasite phase junctions. The band alignment at the phase boundary contributes to the enhanced charge separation and transfer across the interface and the migration of electrons to the pyrite phase accounts for the significant improvement in stability. The controlled introduction of p/m-FeS_2 phase junctions reported here provides a promising approach for designing

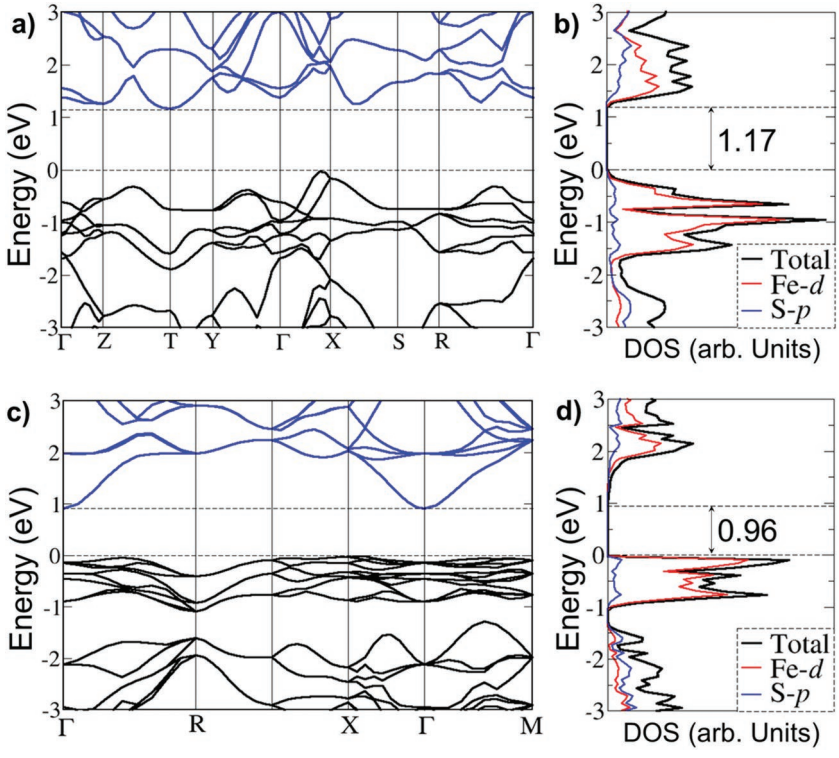

Figure 3. Band structure along the high-symmetry directions of the Brillouin zone of a) marcasite and c) pyrite. Density of states (DOS) of b) marcasite and d) pyrite.

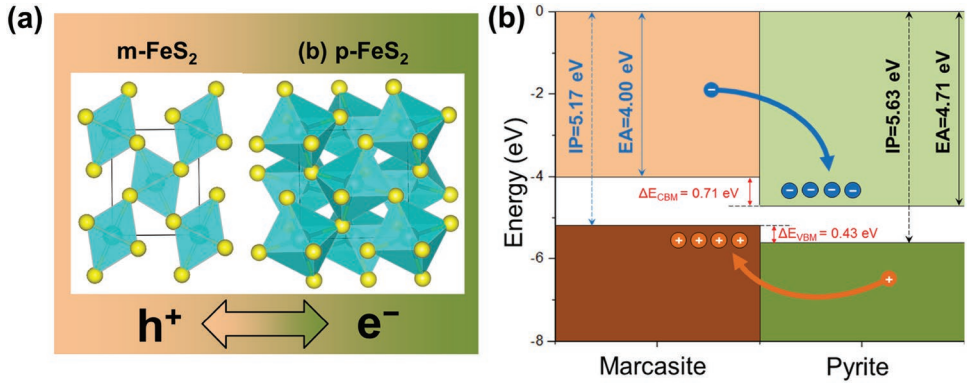

Figure 4. a) Structure of marcasite (left) and pyrite (right) in terms of FeS_6 octahedra. b) Schematic of the band alignment between marcasite and pyrite. IP and EA denote ionization potential and electron affinity, respectively. The electron affinity is calculated by subtracting the band gaps from the calculated ionization potentials. ΔEVBM and ΔECBM are the valence band offsets and conduction band offsets, respectively.

iron sulfide-based PEC cells and will open new avenues for developing more efficient pyrite-based solar cells.

Experimental Section

Mixed Marcasite-Pyrite Films: Preparation of mixed marcasite–pyrite films was done in a home-build thermal chemical vapor deposition/physical vapor deposition (CVD/PVD) system. Particularly, a highly-doped Si wafer with 100 nm thick Fe was placed at specific distance downstream (22, 24 or 26 cm) to the center of the furnace. After loading sulfur powder (500 mg, 99.98%, Aldrich) at the upstream, the tube was sealed and flowed with Ar (50 mL min^{-1} STP) for 15 min. Then the furnace was heated up to 700 °C with a heating rate of 10 °C min^{-1} and the sulfur powder at the upstream of the tube was heated to 170 °C. Under this configuration, it is possible to sulfurize the Fe layer at lower temperature with a stable sulfur partial pressure.[60,61] K-type thermocouples were used to measure the temperature of the film at the specific distance to the center of the furnace. Specifically, distances of 22, 24, and 26 cm correspond to a sulfurization temperature of 455, 380, and 300 °C, respectively. After 5 h sulfurization, FeS_2 films with different marcasite content were obtained (the longer the distance to the center, the lower the temperature).

Characterization: X-ray diffraction patterns were recorded with a Bruker D2 PHASER diffractometer using Cu Kα radiation. SEM images were obtained with a FEI Quanta 200 scanning electron microscope at an accelerating voltage of 5 kV. An accelerating voltage of 15 kV and a Quanta 3D FEG detector was used for EDX analysis. XP spectra were obtained on a ThermoScientific K-Alpha instrument equipped with a monochromatic X-ray source (Al Kα = 1486.6 eV). Energy calibration was performed by using the C 1s peak of adventitious carbon at 284.6 eV as a reference and the spectra were fitted by CasaXPS software. Raman spectra were recorded on a Renishaw InVia^{TM} confocal Raman microscope with a 532 nm laser excitation and 100× objective in the region of 200–1000 cm^{-1}. Raman mapping was done in Streamline mode using a 100× objective with a scan size of 10 × 10 μm^2; the acquisition time per scan was 100 s. The Raman peaks of pyrite and marcasite were fitted with Renishaw WiRE^{TM} using broadened Gaussian/Lorentzian line shapes and corresponding Raman intensity maps were created based on fitted peak areas. UV-Vis-NIR diffuse reflectance spectra were obtained on a Perkin Elmer Lambda 950 UV-Vis-NIR spectrometer single beam instrument over a range of 250–2500 nm.

PEC Measurements: PEC measurements were performed in a three-electrode electrochemical cell with Hg/Hg_2SO_4 as the reference electrode, Pt foil as the counter electrode, and 0.5 M KI as the electrolyte. Chopped light voltammetry *I–V* curves were measured by an Autolab 302N potentiostat, and AM1.5G illumination was provided by a 300 W Xenon lamp (Newport 67005) with an AM1.5G filter. For electrode fabrication, the FeS_2 films on Si wafers were attached on copper wire by conductive silver paste and sealed inside a glass tube with nonconductive epoxy (Hysol 3430 A&B, Loctite) at the end. The epoxy was cured at 60 °C in ambient environment for 1 h, then white lacquer was used to define the active area of electrodes (≈0.3 cm^2). The active area was determined with ImageJ software by using digital images of the electrodes.[62]

Supporting Information

Supporting Information is available from the Wiley Online Library or from the author.

Acknowledgements

M. W. G. M. Verhoeven and L. van Haandel, both from Eindhoven University of Technology, are acknowledged for their assistance in the XPS measurements. A. M. Ganose from University College London is thanked for his assistance in the band alignment calculations. This work is part of the program "CO2-neutral fuels" (project 13-CO26) of the Foundation for Fundamental Research on Matter (FOM), which was financially supported by the Netherlands Organization for Scientific Research (NWO). This research program was co-financed by Shell Global Solutions International B.V. This work made use of the facilities of ARCHER (http://www.archer.ac.uk), the UK's national supercomputing service via our membership of the UK's HEC Materials Chemistry Consortium, which was funded by EPSRC (EP/L000202).

Received: April 26, 2016
Revised: August 8, 2016
Published online: September 15, 2016

[1] a) M. Cabán-Acevedo, N. S. Kaiser, C. R. English, D. Liang, B. J. Thompson, H. E. Chen, K. J. Czech, J. C. Wright, R. J. Hamers, S. Jin, *J. Am. Chem. Soc.* **2014**, *136*, 17163; b) M. Gong, A. Kirkeminde, S. Ren, *Sci. Rep.* **2013**, *3*, 2092; c) J. Xia, J. Jiao, B. Dai, W. Qiu, S. He, W. Qiu, P. Shen, L. Chen, *RSC Adv.* **2013**, *3*, 6132; d) R. Fong, C. H. W. Jones, J. R. Dahn, *J. Power Sources* **1989**, *26*, 333; e) D. Golodnitsky, E. Peled, *Electrochim. Acta* **1999**, *45*, 335.
[2] M. Wang, C. Xing, K. Cao, L. Zhang, J. Liu, L. Meng, *J. Mater. Chem. A* **2014**, *2*, 9496.

[3] X. Qiu, M. Liu, T. Hayashi, M. Miyauchi, K. Hashimoto, *Chem. Commun.* **2013**, *49*, 1232.
[4] L. Samad, M. Cabán-Acevedo, M. J. Shearer, K. Park, R. J. Hamers, S. Jin, *Chem. Mater.* **2015**, *27*, 3108.
[5] a) J. Wu, L. Liu, S. Liu, P. Yu, Z. Zheng, M. Shafa, Z. Zhou, H. Li, H. Ji, Z. M. Wang, *Nano Lett.* **2014**, *14*, 6002; b) S. Bae, D. Kim, W. Lee, *Appl. Catal. B* **2013**, *134*, 93; c) M. Gong, A. Kirkeminde, N. Kumar, H. Zhao, S. Ren, *Chem. Commun.* **2013**, *49*, 9260; d) S. Liu, M. Li, S. Li, H. Li, L. Yan, *Appl. Surf. Sci.* **2013**, *268*, 213; e) A. Ennaoui, H. Tributsch, *Sol. Cells* **1984**, *13*, 197.
[6] a) A. Ennaoui, S. Fiechter, W. Jaegermann, H. Tributsch, *J. Electrochem. Soc.* **1986**, *133*, 97; b) H. A. Macpherson, C. R. Stoldt, *ACS Nano* **2012**, *6*, 8940; c) Y. Bi, Y. Yuan, C. L. Exstrom, S. A. Darveau, J. Huang, *Nano Lett.* **2011**, *11*, 4953.
[7] A. Ennaoui, S. Fiechter, C. Pettenkofer, N. Alonso-Vante, K. Büker, M. Bronold, C. Höpfner, H. Tributsch, *Sol. Energy Mater. Sol. Cells* **1993**, *29*, 289.
[8] N. Berry, M. Cheng, C. L. Perkins, M. Limpinsel, J. C. Hemminger, M. Law, *Adv. Energy Mater.* **2012**, *2*, 1124.
[9] S. Shukla, N. H. Loc, P. P. Boix, T. M. Koh, R. R. Prabhakar, H. K. Mulmudi, J. Zhang, S. Chen, C. F. Ng, C. H. A. Huan, N. Mathews, T. Sritharan, Q. Xiong, *ACS Nano* **2014**, *8*, 10597.
[10] Y.-C. Wang, D.-Y. Wang, Y.-T. Jiang, H.-A. Chen, C.-C. Chen, K.-C. Ho, H.-L. Chou, C.-W. Chen, *Angew. Chem. Int. Ed.* **2013**, *52*, 6694.
[11] a) J. M. Lucas, C. C. Tuan, S. D. Lounis, D. K. Britt, R. Qiao, W. Yang, A. Lanzara, A. P. Alivisatos, *Chem. Mater.* **2013**, *25*, 1615; b) H. Xian, J. Zhu, X. Liang, H. He, *RSC Adv.* **2016**, *6*, 31988; c) Y. Bai, J. Yeom, M. Yang, S. H. Cha, K. Sun, N. A. Kotov, *J. Phys. Chem. C* **2013**, *117*, 2567; d) L. Zhu, B. J. Richardson, Q. Yu, *Chem. Mater.* **2015**, *27*, 3516.
[12] a) V. Antonucci, A. S. Arico', N. Giordano, P. L. Antonucci, U. Russo, D. L. Cocke, F. Crea, *Sol. Cells* **1991**, *31*, 119; b) C. W. Lin, D. Y. Wang, Y. T. Wang, C. C. Chen, Y. J. Yang, Y. F. Chen, *Sol. Energy Mater. Sol. Cells* **2011**, *95*, 1107.
[13] J. Puthussery, S. Seefeld, N. Berry, M. Gibbs, M. Law, *J. Am. Chem. Soc.* **2011**, *133*, 716.
[14] M. Limpinsel, N. Farhi, N. Berry, J. Lindemuth, C. L. Perkins, Q. Lin, M. Law, *Energy Environ. Sci.* **2014**, *7*, 1974.
[15] L. P. Yu, S. Lany, R. Kykyneshi, V. Jieratum, R. Ravichandran, B. Pelatt, E. Altschul, H. A. S. Platt, J. F. Wager, D. A. Keszler, A. Zunger, *Adv. Energy Mater.* **2011**, *1*, 748.
[16] S. Seefeld, M. Limpinsel, Y. Liu, N. Farhi, A. Weber, Y. Zhang, N. Berry, Y. J. Kwon, C. L. Perkins, J. C. Hemminger, R. Wu, M. Law, *J. Am. Chem. Soc.* **2013**, *135*, 4412.
[17] S. Shukla, G. Xing, H. Ge, R. R. Prabhakar, S. Mathew, Z. Su, V. Nalla, T. Venkatesan, N. Mathews, T. Sritharan, T. C. Sum, Q. Xiong, *ACS Nano* **2016**, *10*, 4431.
[18] R. Murphy, D. R. Strongin, *Surf. Sci. Rep.* **2009**, *64*, 1.
[19] D. Liang, M. Cabán-Acevedo, N. S. Kaiser, S. Jin, *Nano Lett.* **2014**, *14*, 6754.
[20] M. S. Jagadeesh, M. S. Seehra, *Phys. Lett. A* **1980**, *80*, 59.
[21] C. Wadia, Y. Wu, S. Gul, S. K. Volkman, J. Guo, A. P. Alivisatos, *Chem. Mater.* **2009**, *21*, 2568.
[22] D. Schleich, H. Chang, *J. Cryst. Growth* **1991**, *112*, 737.
[23] M. S. Schmøkel, L. Bjerg, S. Cenedese, M. R. V. Jørgensen, Y. S. Chen, J. Overgaard, B. B. Iversen, *Chem. Sci.* **2014**, *5*, 1408.
[24] V. K. Gudelli, V. Kanchana, S. Appalakondaiah, G. Vaitheeswaran, M. C. Valsakumar, *J. Phys. Chem. C* **2013**, *117*, 21120.
[25] C. Sánchez, E. Flores, M. Barawi, J. M. Clamagirand, J. R. Ares, I. J. Ferrer, *Solid State Commun.* **2016**, *230*, 20.
[26] Z. Ding, G. Q. Lu, P. F. Greenfield, *J. Phys. Chem. B* **2000**, *104*, 4815.
[27] H. Tahiri, N. Serpone, R. L. van Mao, *J. Photochem. Photobiol. A* **1996**, *93*, 199.
[28] T. Kawahara, Y. Konishi, H. Tada, N. Tohge, J. Nishii, S. Ito, *Angew. Chem.* **2002**, *114*, 2935.
[29] D. O. Scanlon, C. W. Dunnill, J. Buckeridge, S. A. Shevlin, A. J. Logsdail, S. M. Woodley, C. R. A. Catlow, M. J. Powell, R. G. Palgrave, I. P. Parkin, G. W. Watson, T. W. Keal, P. Sherwood, A. Walsh, A. A. Sokol, *Nat. Mater.* **2013**, *12*, 798.
[30] P. Deák, B. Aradi, T. Frauenheim, *J. Phys. Chem. C* **2011**, *115*, 3443.
[31] M.-G. Ju, G. Sun, J. Wang, Q. Meng, W. Liang, *ACS Appl. Mater. Interfaces* **2014**, *6*, 12885.
[32] Y. Nosaka, A. Y. Nosaka, *J. Phys. Chem. Lett.* **2016**, *7*, 431.
[33] X. Wang, Q. Xu, M. Li, S. Shen, X. Wang, Y. Wang, Z. Feng, J. Shi, H. Han, C. Li, *Angew. Chem. Int. Ed.* **2012**, *51*, 13089.
[34] M. G. Ju, X. Wang, W. Z. Liang, Y. Zhao, C. Li, *J. Mater. Chem. A* **2014**, *2*, 17005.
[35] M.-G. Ju, X. Wang, W. Liang, Y. Zhao, C. Li, *J. Mater. Chem. A* **2014**, *2*, 17005.
[36] R. Sun, M. K. Y. Chan, G. Ceder, *Phys. Rev. B* **2011**, *83*, 235311.
[37] D. Spagnoli, K. Refson, K. Wright, J. D. Gale, *Phys. Rev. B* **2010**, *81*, 094106.
[38] I. Uhlig, R. Szargan, H. W. Nesbitt, K. Laajalehto, *Appl. Surf. Sci.* **2001**, *179*, 222.
[39] S. L. Harmer, H. W. Nesbitt, *Surf. Sci.* **2004**, *564*, 38.
[40] X. Zhang, M. Manno, A. Baruth, M. Johnson, E. S. Aydil, C. Leighton, *ACS Nano* **2013**, *7*, 2781.
[41] A. R. Lennie, D. J. Vaughan, *Am. Mineral.* **1992**, *77*, 1166.
[42] A. Pascual, S. Yoda, M. Barawi, J. M. Clamagirand, J. R. Ares, I. J. Ferrer, *J. Phys. Chem. C* **2014**, *118*, 26440.
[43] M. Cabán-Acevedo, D. Liang, K. S. Chew, J. P. DeGrave, N. S. Kaiser, S. Jin, *ACS Nano* **2013**, *7*, 1731.
[44] M. Cabán-Acevedo, M. S. Faber, Y. Tan, R. J. Hamers, S. Jin, *Nano Lett.* **2012**, *12*, 1977.
[45] A. López, R. L. Frost, *J. Raman Spectrosc.* **2015**, *46*, 1033.
[46] S. Middya, A. Layek, A. Dey, P. P. Ray, *J. Mater. Sci. Technol.* **2014**, *30*, 770.
[47] J. P. Perdew, K. Burke, M. Ernzerhof, *Phys. Rev. Lett.* **1996**, *77*, 3865.
[48] V. I. Anisimov, F. Aryasetiawan, A. I. Lichtenstein, *J. Phys.: Condens. Matter* **1997**, *9*, 767.
[49] J. Hu, Y. Zhang, M. Law, R. Wu, *J. Am. Chem. Soc.* **2012**, *134*, 13216.
[50] P. Xiao, X.-L. Fan, L.-M. Liu, W.-M. Lau, *Phys. Chem. Chem. Phys.* **2014**, *16*, 24466.
[51] Y. N. Zhang, J. Hu, M. Law, R. Q. Wu, *Phys. Rev. B* **2012**, *85*, 085314.
[52] J. Hu, Y. Zhang, M. Law, R. Wu, *Phys. Rev. B* **2012**, *85*, 085203.
[53] T. Schena, G. Bihlmayer, S. Blügel, *Phys. Rev. B* **2013**, *88*, 235203.
[54] J. Hu, Y. Zhang, M. Law, R. Wu, *J. Am. Chem. Soc.* **2012**, *134*, 13216.
[55] P. Xiao, X.-L. Fan, L.-M. Liu, W.-M. Lau, *Phys. Chem. Chem. Phys.* **2014**, *16*, 24466.
[56] A. Schlegel, P. Wachter, *J. Phys. C: Solid State Phys.* **1976**, *9*, 3363.
[57] M. E. Fleet, *Can. Mineral.* **1970**, *10*, 225.
[58] K. J. Brock, L. J. Slater, *Am. Mineral.* **1978**, *63*, 210.
[59] B. Thomas, T. Cibik, C. Höpfner, K. Diesner, G. Ehlers, S. Fiechter, K. Ellmer, *J. Mater. Sci.: Mater. Electron.* **1998**, *9*, 61.
[60] G. Pimenta, W. Kautek, *Thin Solid Films* **1992**, *219*, 37.
[61] S. Rakib, M. Gendry, P. Klopfenstein, R. Saoudi, J. Durand, *Thin Solid Films* **1990**, *187*, 309.
[62] L. Gao, Y. Cui, R. H. J. Vervuurt, D. van Dam, R. P. J. van Veldhoven, J. P. Hofmann, A. A. Bol, J. E. M. Haverkort, P. H. L. Notten, E. P. A. M. Bakkers, E. J. M. Hensen, *Adv. Funct. Mater.* **2016**, *26*, 679.